Solution Structure of Zinc- and Calcium-Bound Rat S100B as Determined by Nuclear Magnetic Resonance Spectroscopy†,‡

Paul T. Wilder,§ Kristen M. Varney,|| Michele B. Weiss,§ Rossitza K. Gitti,|| and David J. Weber*,§,||

Molecular and Cell Biology Program, Department of Biochemistry and Molecular Biology, University of Maryland School of Medicine, 108 North Greene Street, Baltimore, Maryland 21201

Received November 16, 2004; Revised Manuscript Received February 21, 2005

ABSTRACT: The EF-hand calcium-binding protein S100B also binds one zinc ion per subunit with a relatively high affinity ($K_d \sim 90$ nM) [Wilder et al., (2003) *Biochemistry 42*, 13410−13421]. In this study, the structural characterization of zinc binding to calcium-loaded S100B was examined using high-resolution NMR techniques, including structural characterization of this complex in solution at atomic resolution. As with other S100 protein structures, the quaternary structure of Zn^{2+}-Ca^{2+}-bound S100B was found to be dimeric with helices H1, H1′, H4, and H4′ forming an X-type four-helix bundle at the dimer interface. NMR data together with mutational analyses are consistent with Zn^{2+} coordination arising from His-15 and His-25 of one S100B subunit and from His-85 and Glu-89 of the other subunit. The addition of Zn^{2+} was also found to extend helices H4 and H4′ three to four residues similar to what was previously observed with the binding of target proteins to S100B. Furthermore, a kink in helix 4 was observed in Zn^{2+}-Ca^{2+}-bound S100B that is not in Ca^{2+}-bound S100B. These structural changes upon Zn^{2+}-binding could explain the 5-fold increase in affinity that Zn^{2+}-Ca^{2+}-bound S100B has for peptide targets such as the TRTK peptide versus Ca^{2+}-bound S100B. There are also changes in the relative positioning of the two EF-hand calcium-binding domains and the respective helices comprising these EF-hands. Changes in conformation such as these could contribute to the order of magnitude higher affinity that S100B has for calcium in the presence of Zn^{2+}.

S100B and other members of the S100 protein family have a conserved N-terminal S100 "pseudo" EF-hand and a C-terminal "typical" EF-hand Ca^{2+}-binding motif (*1*, *2*). Upon binding Ca^{2+}, most dimeric S100 proteins undergo a conformational change that regulates their binding to target proteins as necessary for modulating numerous biological functions (*3*, *4*). In addition, S100B and several other S100 proteins bind Zn^{2+} in a site unique from the Ca^{2+}-binding site (*5*). For example, Ca^{2+}-bound S100B symmetrically binds two Zn^{2+} per dimer ($K_d = 94.2 \pm 16.7$ nM), with both zinc-binding sites having liganding residues contributed from each subunit at the dimer interface (*6*). While the biological function of Zn^{2+} in S100 proteins is not completely understood, these divalent ions are not structural elements because the proteins are stable, folded, and active *in vitro* in their absence. Instead, it is more likely that Zn^{2+} plays a regulatory role by modulating the affinity of various S100 proteins for Ca^{2+} and/or protein targets. In the case of S100B, the binding affinity of Ca^{2+} increases by as much as 10-fold (*7*) and its affinity for a peptide derived from the protein CapZ (TRTK)[1] increases 5-fold (*8*) when Zn^{2+} is present. Likewise, the Ca^{2+}-dependent binding of peptides derived from giant phosphoprotein AHNAK to S100B is enhanced by the presence of Zn^{2+} (*9*).

Other S100 family members also bind Zn^{2+} including S100A2 ($K_d = 4.6$ μM), S100A3 ($K_d = 1.5$ μM), S100A4 (affinity not reported), S100A5 ($[Zn^{2+}]_{0.5} = 2$ μM), S100A6 ($K_d = 0.1$ μM), and S100A7 ($K_d = 100$ μM) (*10*), and in each case, a conformational change is observed upon binding Zn^{2+} ions. S100A12 binds Zn^{2+} with relatively high affinity ($K_d < 10$ nM) compared to other S100 proteins causing a large increase (∼1500-fold) in its affinity for Ca^{2+} (*11*). The S100B/S100A1 heterodimer and S100A1 are also capable of binding Zn^{2+} but with a lower affinity than the S100B homodimer (S100B > S100B/A1 > S100A1) (*12*). Nonethe-

† This work was supported by grants from the National Institutes of Health (GM58888, to D.J.W.).

‡ Coordinates for the 20 best structures of rat Zn^{2+}-Ca^{2+}-S100B and the associated restraint files have been deposited in the Brookhaven Protein Data Bank under the PDB code 1XYD.

* To whom correspondence should be addressed: Department of Biochemistry and Molecular Biology, University of Maryland School of Medicine, 108 N. Greene St., Baltimore, Maryland 21201. Telephone: (410) 706-4354. Fax: (410) 706-0458. E-mail: dweber@umaryland.edu.

§ Molecular and Cell Biology Program.

|| Department of Biochemistry and Molecular Biology.

[1] Abbreviations: ITC, isothermal titration calorimetry; NMR, nuclear magnetic resonance; TRTK, CapZα peptide (^{265}TRTKIDWNKILS^{276}); NDR, nuclear serine/threonine kinase peptide (^{62}KRLRRSAHARKETEFLRLKRTRLGLE^{87}); ACS, American Chemical Society; p53$^{367-388}$, human p53 peptide (^{367}SHLKSKKGQSTSRHKKLMFKTE^{388}); p53^{F385W}, fluorescent p53 peptide (^{367}SHLKSKKGQSTSRHKKLMWKTE^{388}); DTT, dithiothreitol; TES, (2-[(2-hydroxy-1,1-bis[hydroxymethyl]ethyl)-amino]ethanesulfonic acid); TPPI, time-proportional phase incrementation; TSP, 3-(trimethylsilyl)-propionic acid-D4, sodium salt; HSQC, heteronuclear single-quantum coherence; NOESY, nuclear Overhauser effect spectroscopy; HOHAHA, homonuclear Hartman−Hahn spectroscopy; HMQC, heteronuclear multiple-quantum coherence; DIPSI-2, decoupling in the presence of scalar interaction version 2; EDTA, ethylenediaminetetraacetic acid; BMRB, BioMagResBank; rmsd, root-mean-square difference; PDB, Protein Data Bank; WT, wild type; 3D, three-dimensional; TPEN, *N*,*N*,*N*′,*N*′-tetrakis(2-pyridylmethyl)ethylenediamine.

10.1021/bi0475830 CCC: $30.25
Published on Web 03/22/2005

less, when Zn^{2+} is bound to S100A1, it has a higher binding affinity for synapsin IIa when Zn^{2+} is bound (*13*). S100A9, another calcium/zinc binding S100 protein, was found to compete with S100B for Zn^{2+} in gel-binding assays (*14*), and when S100A9 forms a heterodimer with S100A8, Zn^{2+}-binding modulates binding to arachidonic acid (*15*) and the antimicrobial activity of the S100A8/A9 heterodimer (*16*).

A comparison of the X-ray crystal structures of Zn^{2+}-Ca^{2+}-S100A7 (*17*) and Cu^{2+}-Ca^{2+}-S100A12 (*18*) illustrates that Zn^{2+} and Cu^{2+} bind to a similarly located binding site on S100 proteins. As found for S100B, S100A7 also coordinates Zn^{2+} with residues from the C terminus of one subunit and from residues in the pseudo-EF-hand of the other subunit at the dimer interface. Likewise, Zn^{2+} and Cu^{2+} bound to S100A7 and S100A12, respectively, are both coordinated using residues analogous to those in S100B based on mutational analysis and NMR data (*6*). While it is not yet known whether Zn^{2+}-bound S100A7 has a higher affinity for Ca^{2+} than in its absence, Ca^{2+} bound to the pseudo-EF-hand and the typical-EF-hands are closer together, and a slight change in conformation in the pseudo-EF-hand upon binding Zn^{2+} is observed (*17*). A similar result was discovered for S100B using fluorescence energy-transfer measurements (*19*), which may be related to its increased calcium-binding affinity when Zn^{2+} is bound.

Building upon previously determined sequence-specific assignments of S100B and its secondary structure determination (*6*), the high-resolution NMR structure of Zn^{2+}-Ca^{2+}-S100B was completed as described in this paper. This novel structure is compared to the other S100B solution NMR structures including apo-S100B (*20*), Ca^{2+}-S100B (*21*), $p53^{367-388}$-bound S100B (*22*), TRTK-bound S100B (*23*), NDR-bound S100B (*24*), and the X-ray crystal structures of Cu^{2+}-Ca^{2+}-S100A12 (*18*) and Zn^{2+}-Ca^{2+}-S100A7 (*17*). Such comparisons are useful for identifying changes in S100B upon Zn^{2+} binding that may modulate Ca^{2+} affinity for this EF-hand-containing protein. The structure reported here for Zn^{2+}-Ca^{2+}-S100B is also useful for understanding how Zn^{2+}-binding changes the structure of S100B and mediates its calcium-dependent protein−protein interactions.

MATERIALS AND METHODS

Materials. All chemicals and reagents were ACS-grade or higher and purchased from Sigma−Aldrich unless otherwise indicated, and all buffers were passed through Chelex-100 resin to remove trace metals. $^{15}NH_4Cl$ and ^{13}C-labeled glucose were purchased from Cambridge Isotope Laboratories (Woburn, MA).

Preparation of Wild-Type and Mutant S100B. A pET11b (Novagen, Inc., Madison, WI) expression vector containing the rat S100B gene, as described previously (*2*), was used for production of unlabeled, ^{15}N-labeled, and ^{13}C,^{15}N-labeled S100B. Mutations in the S100B protein (H15A, D23A, H25A, C84A, H85A, E89A, and the Δ89−91) were made using Quick-Change Mutagenesis Kit (Stratagene, Inc., La Jolla, CA), as described previously (*6*). Wild-type and mutant proteins were prepared and purified (>99%) under reducing conditions using procedures similar to those described previously (*2*, *6*, *25*), except DTT was used as a reducing agent instead of β-mercaptoethanol. The concentrations of wild-type and mutant S100B stock solutions were determined using the Bio-Rad Protein Assay (Bio-Rad) using wild-type S100B of known concentration as the standard. The concentration of this S100B standard was determined by amino acid analysis (Commonwealth Biotechnologies, Inc., Richmond, VA). The concentrated purified protein was stored at a concentration of 1−7 mM in 2 mM TES at pH 7.2, with 0.5 mM DTT at −20 °C until use.

The NMR samples contained 3 mM ^{15}N- or ^{13}C,^{15}N-labeled S100B subunit, 3 mM zinc acetate, 10 mM $CaCl_2$, 0.34 mM NaN_3, 15 mM NaCl, <0.07 mM DTT, 10 mM TES at pH 7.2, and 10% D_2O, except the LR-HSQC sample contained 1 mM ^{15}N-labeled S100B subunit, 1 mM zinc acetate, 3.3 mM $CaCl_2$, 0.34 mM NaN_3, 15 mM NaCl, <0.07 mM DTT, 10 mM TES at pH 7.2, and 10% D_2O. Samples prepared in this manner were stable for more than 2 weeks at 37 °C.

For aligned samples, necessary to collect residual dipolar coupling, Zn^{2+}-Ca^{2+}-bound-S100B was prepared in radially compressed (stretched) polyacrylamide gels as previously described (*26*, *27*). Briefly, polyacrylamide gels were prepared to a final polyacrylamide concentration of 5.5% and cast in a gel stretcher apparatus (New Era Enterprises, Inc.) (*26*). After the gel was allowed to polymerize, it was washed in doubly distilled deionized water for 1 h (3×) and soaked in the NMR buffer described above without S100B. The gel was then cut to 10 mm and soaked overnight in 400 μL of 1.3 mM S100B in the above NMR buffer plus 20% D_2O and 0.4 mM sodium azide. The next day, the gel was placed into a stretching apparatus, forced through a funnel, and into an open-ended 5 mm NMR tube, which results in stretching the gel from 10 to 20 mm in length by radial compression. The bottom of the tube was sealed, and a plunger was placed on the top of the tube and sealed with a cap and Parafilm prior to data collection.

Isothermal Titration Calorimetry (ITC). Binding of Zn^{2+} to wild-type and mutant S100B was analyzed by measuring heat changes during the titration of zinc acetate into the protein solution using a VP-ITC titration microcalorimeter (MicroCal, Inc., Northhampton, MA) as done previously (*6*). Briefly, all protein and metal-ligand solutions were degassed under vacuum and equilibrated at 37 °C prior to titration. The sample cell (1.4 mL) contained 10 mM TES at pH 7.2, 15 mM NaCl, and 10 mM $CaCl_2$, with either 0.2 mM wild-type, mutant S100B, or no protein, while the reference cell contained water. Upon equilibration, a 1.50, 3.75, 5.00, or 15.00 mM zinc acetate solution prepared in the same buffer without S100B was injected in 5 μL aliquots using the default injection rate with a 300 s interval between each injection to allow the sample to return to baseline. The resulting titration curves were corrected for the protein-free buffer control and analyzed using the Origin for ITC software supplied by MicroCal (Northampton, MA).

NMR Spectroscopy. NMR experiments performed for the sequence-specific resonance assignment and structure determination of Zn^{2+}-Ca^{2+}-S100B are described previously (*28*). For additional assignments and for structural data, heteronuclear NMR spectra were collected at 37 °C with either a Bruker DMX600 NMR spectrometer (600.13 MHz for protons) equipped with four frequency channels and a triple-resonance three-axis gradient probe, the same Bruker DMX600 NMR spectrometer (600.13 MHz for protons) equipped with four frequency channels and a triple-resonance *z*-axis gradient 5 mM cryoprobe, or a Bruker AVANCE 800

NMR spectrometer (800.27 MHz for protons) equipped with four frequency channels and a triple-resonance *z*-axis gradient 5 mM cryoprobe. Unless otherwise stated, a 1 s relaxation delay was used and quadrature detection in the indirect dimensions was obtained with States-TPPI phase cycling (*29*). For most experiments, initial delays in the indirect dimensions were set to give zero- and first-order phase corrections of 90° and −180°, respectively (*30*). Data were processed using the processing program nmrPipe (*31*). Time-domain data in the indirect dimensions were extended by no more than one-third using standard linear prediction routines (*32*), except for data in constant time domains that were extended 2-fold using mirror-image linear prediction (*33*). All proton chemical shifts are reported with respect to the H_2O or HDO signal taken to be 4.658 ppm relative to external TSP (0.0 ppm) at 37 °C. The ^{13}C and ^{15}N chemical shifts were indirectly referenced using the following ratios of the zero-point frequencies at 37 °C: 0.101 329 05 for ^{15}N-^{1}H and 0.251 449 53 for ^{13}C-^{1}H (*34*−*36*).

Specifically, uniformly ^{15}N-labeled S100B was used to collect the 2D ^{1}H,^{15}N-fast HSQC (*37*), 2D ^{1}H,^{15}N-long-range HSQC (*38*), 3D ^{15}N-edited NOESY−HSQC, 3D ^{15}N-edited HOHAHA-HSQC (*29*, *37*), 3D ^{15}N,^{15}N-edited HMQC−NOESY−HSQC (*39*), 3D HNHA (*40*), and 2D IPAP ^{1}H-^{15}N HSQC (*41*). A ^{13}C,^{15}N-labeled S100B was used to collect 3D CBCA(CO)NH (*42*), 3D HNCACB (*43*), 3D HNCA (*44*), 3D HNCO (*44*), 3D C(CO)NH (*45*), 4D ^{13}C,^{15}N-edited NOESY−HSQC (*46*), and 4D ^{13}C,^{13}C-edited NOESY−HSQC (*47*). For the HNCACB experiment, a longer delay (7.2 ms) was used to transfer magnetization solely to C_β prior to carbon data acquisition rather than the shorter delay (3.6 ms) that is more typically used for collection of both C_α and C_β data, as previously described (*43*). The fast-HSQC detection scheme was incorporated in most of the pulse sequences, and pulse-field gradients were used as needed to purge undesired magnetization (*48*).

Structure Calculations. Interproton distance restraints were derived from NOE cross-peaks and classified into five levels including strong, medium, medium weak, weak, and very weak, and the NOEs were then assigned distance constraints with a lower limit of 1.8 Å and an upper limit of 2.9, 3.5, 4.2, 5, and 6 Å, respectively (*49*). Pseudoatom corrections were applied to the upper limit for degenerate methyl, methylene, and aromatic ring protons (*50*, *51*) and constraints for methyl protons were shifted down one category as described previously (*50*, *51*). Only structurally useful constraints were used; therefore, NOE correlations between geminal protons and between vicinal methylene protons were not used for constraints. A total of 98 internuclear dipolar couplings (in hertz) were determined from the difference in J splitting between the isotropic and aligned phases of the 2D IPAP−HSQC data. The axial ($\mathbf{A}_a$) and rhombic ($\mathbf{A}_r$) components of the alignment tensor **A** were obtained from a histogram of the dipolar couplings as described previously (*52*). The force constants for the dipolar coupling energies were slowly increased in concert with the force constant of the NOE energy during the cooling stage of the structure calculations. The initial force constants used were typically very small (0.001 kcal Hz^{-2}), and the final force constants were determined for the $^{1}D_{NH}$ dipolar couplings such that the calculated structures represented the estimated uncertainty in the actual dipolar coupling data set as previously described (*20*). Dihedral constraint ϕ angles were calculated from $^{3}J_{NH-H\alpha}$ coupling constants determined using data from the 3D HNHA (*40*). These values agreed with values determined using TALOs, which was used to predict both ϕ and ψ angles based on the chemical-shift data (*53*). In regions of known secondary structure, the values were within the ideal values for α helices ($\phi = -60 \pm 20°$, $\psi = -40 \pm 15°$) and β sheets ($\phi = -120 \pm 30°$, $\psi = 140 \pm 30°$) and the dihedral values determined for the typical EF-hand also agreed well with values determined by the averaging of 11 crystal structures of typical EF-hands (*54*). Backbone hydrogen-bond constraints of $r_{NH-O} = 1.5-2.8$ Å and $r_{N-O} = 2.4-3.5$ Å were included in the regions of known secondary structure in the final stages of structure determination (*6*); however, when these constraints are left out, there is no statistical affect on the ensemble of structures. Distance constraints from Ca^{2+} to protein ligands of 2.0−2.8 Å were introduced as described previously for determining the NMR structure of Ca^{2+}-S100B (*21*) and were consistent with that observed in the X-ray crystal structure (*55*). Constraints to Zn^{2+} were not used in any of the initial structure calculations of Zn^{2+}-Ca^{2+}-S100B.

Structures were calculated using XPLOR-NIH, version 2.9.7, running on Linux using standard protocols for sub-structure embedding and regularization, hybrid distance geometry-simulated annealing (DGSA) regularization and refinement, and simulated annealing (SA) refinement (*56*). A conformational database potential and pseudopotentials for secondary $^{13}C^{\alpha}$ and $^{13}C^{\beta}$ chemical shifts were included in the SA refinement. To keep the symmetry of the homodimer intact, noncrystallographic symmetry (NCS) and distance symmetry constraints with force constants of 100 and 1 kcal mol^{-1} $Å^{-2}$, respectively, were employed using DGSA and SA routines. The refinement process yielded many structures with no distance constraint violations greater than 0.4 Å and no dihedral constraint violations of greater than 5°.

Zn^{2+}-Binding Constraints. Once high-quality structures were calculated without Zn^{2+} constraints, the inclusion of ligands to Zn^{2+} was examined. Specifically, structures were calculated using XPLOR-NIH as outlined above, except that addition distance constraints from Zn^{2+} to the putative Zn^{2+} ligands were introduce as pseudo-NOEs with a S−Zn^{2+} distance of 2.3 Å (Cys), N−Zn^{2+} distance of 2.0 Å (His), O−Zn^{2+} distance of 2.04 Å for monodentate ligands (Glu, Asp, and backbone carbonyls), and O−Zn^{2+} distance of 2.2 Å for bidentate ligands (Glu and Asp). These distances are based on the average ligand−Zn^{2+} distances determined from ≤1.6 Å resolution crystal structures found in the Protein Data Bank (PDB) (*57*). LR-HSQC data was used to establish the tautomerization of the His imidazole ring and to determine whether the His $N^{\epsilon 2}$ or $N^{\delta 1}$ is coordinating Zn^{2+} as previously described (*20*). The 20 lowest energy structures generated using different combinations of putative Zn^{2+} ligands without distance constraint violations greater than 0.4 Å and no dihedral constraint violations of greater than 5° were then compared to the 20 lowest energy structures generated without distance constraints to Zn^{2+} to judge the quality of structures. The extent to which the geometry of the Zn^{2+} coordination was close to an ideal for coordinating Zn^{2+} as a tetrahedron (for 4 ligands) or trigonal bipyramid (for 5 ligands) was also used to judge whether the Zn^{2+} ligands were reasonable.

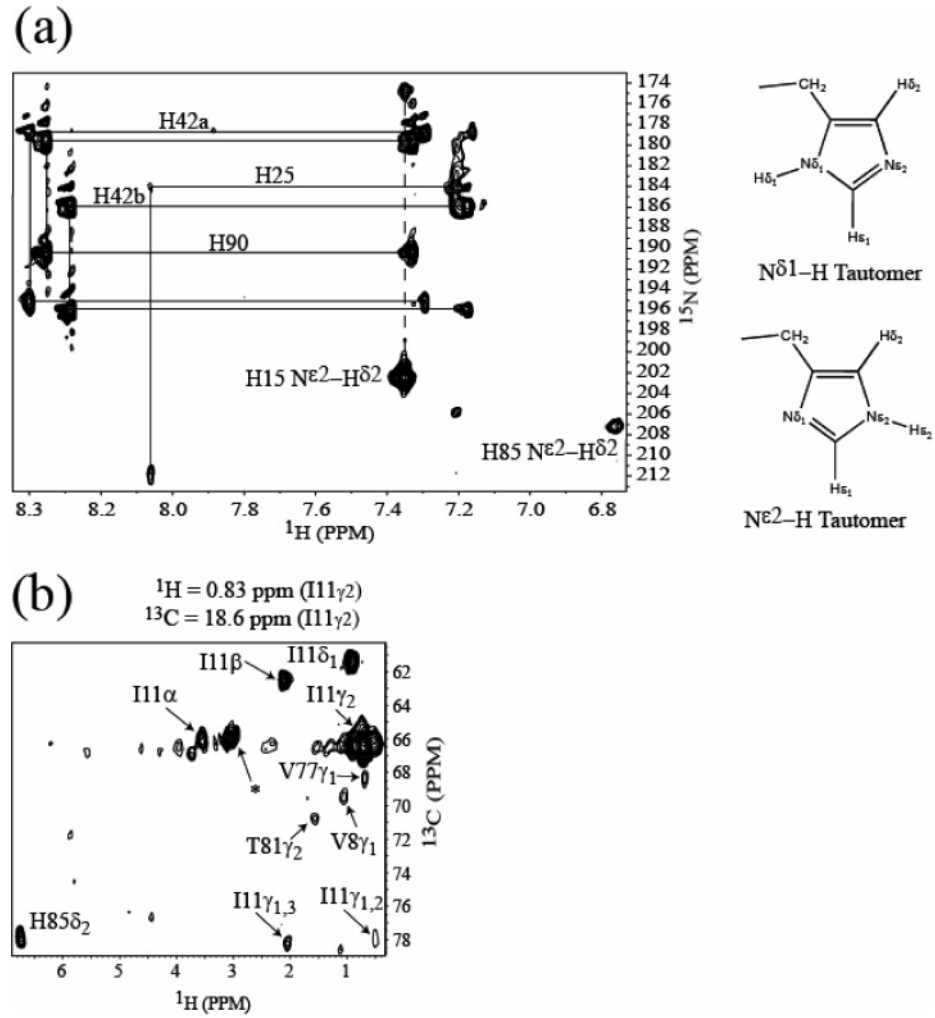

FIGURE 1: NMR spectra illustrating correlations to Histidine residues on Zn^{2+}-Ca^{2+}-S100B. (a) Long-range HSQC spectrum (LR-HSQC) of Zn^{2+}-Ca^{2+}-S100B that was used for the assignment of side-chain resonances and the tautomerization state of the His imidazoles. His-15 and His-85 lock into the $N^{\delta 1}$ tautomerization state, and His-25 locks into the $N^{\epsilon 2}$ tautomerization state. His-90 and His-42, which do not ligand Zn^{2+}, do not strongly favor one or the other tautomer. (b) Plane from the 4D ^{13}C,^{13}C-edited NOESY spectrum showing NOE correlations from I11−$H^{\gamma 2}$ in helix I to V77−$H^{\gamma 1}$, T81−H^{γ}, and H85−$H^{\gamma 2}$. The identification of H85−$H^{\delta 2}$ and other His imidazole protons in the 4D ^{13}C,^{13}C-edited NOESY allowed the assignment of correlations in the LR-HSQC and provided NOE correlations that were useful for orienting His side chains in the solution structure determination of Zn^{2+}-Ca^{2+}-S100B.

RESULTS AND DISCUSSION

Resonance Assignments and Tautomerization of His Residues in Zn^{2+}-Ca^{2+}-S100B. Chemical-shift assignments (^1H, ^{13}C, and ^{15}N) for Zn^{2+}-Ca^{2+}-S100B were made using standard heteronuclear multiple dimensional NMR spectroscopic techniques as described previously (*6*). However, additional experiments were completed here that made it possible to complete the resonance and NOE assignments as necessary to determine the 3D solution structure of Zn^{2+}-Ca^{2+}-S100B. The assignment of His side-chain residues is particularly important and was made for Zn^{2+}-Ca^{2+}-S100B using the His side-chain assignments of Ca^{2+}-S100B as a starting point (*6*). In the absence of Zn^{2+}, the side-chain His resonances for His-15, His-25, His-42, and His-90 were readily assigned, whereas correlations for His-85 were missing, likely because of exchange broadening effects in the apo- and Ca^{2+}-bound states of wild-type S100B (*6*). Upon the addition of Zn^{2+} to Ca^{2+}-S100B, all of the observable $^{15}N^{\delta 1}/^{15}N^{\epsilon 2}$ to carbon-attached $^1H^{\delta 2}/^1H^{\epsilon 1}$ side-chain correlations of the His residues broadened and shifted as observed in long-range HSQC (LR-HSQC) NMR experiments such that the resonances of His-15 and His-25 side chains disappeared completely (H15 > H25 > H42 > H90). At later stages of the titration, the correlations for His-90 and His-42 narrowed and new correlations reappeared in the slow-exchange regime, making it necessary to reassign the LR-HSQC spectrum *a priori* for Zn^{2+}-Ca^{2+}-S100B (Figure 1). The resonance assignments in the LR-HSQC could be made in a straightforward manner by examining intraresidue and sequential NOE correlations from ^{13}C-attached $^1H^{\delta 2}/^1H^{\epsilon 1}$ protons of the His side chains to ^{13}C-attached protons of the backbone (^1H-$^{13}C_{\alpha}$, ^1H-$^{13}C_{\beta}$, etc.) in a 4D ^{13}C,^{13}C-edited NOESY experiment. Interestingly, a LR-HSQC correlation for His-85 appeared and could now be assigned, as well as the side-chain resonances for the remaining His residues in Zn^{2+}-Ca^{2+}-S100B. The 4D ^{13}C,^{13}C-edited NOESY data set was also useful for identifying long-range ^1H-^1H NOE constraints to the side-chain protons of His residues, which helped define the location of several side-chain moieties in the Zn^{2+}-binding side. For example, Figure 1b illustrates long-range NOE correlations from Ile-11γ of Zn^{2+}-Ca^{2+}-S100B to the side-chain $\delta 2$ proton of His-85. An amendment

Table 1: NMR-Derived Restraints and Statistics of NMR Structures[a]

	with Zn^{2+} constraints		without Zn^{2+} constraints	
	⟨20⟩	best	⟨20⟩	best
rmsd from distance constraints (Å)[b]				
total (2626/2618)[c]	0.032 ± 0.001	0.031	0.032 ± 0.001	0.032
intraresidue (478)	0.016 ± 0.006	0.016	0.017 ± 0.005	0.005
sequential (576)	0.018 ± 0.003	0.020	0.018 ± 0.003	0.022
medium range (692)	0.047 ± 0.002	0.045	0.046 ± 0.003	0.049
long range (418)	0.032 ± 0.004	0.022	0.032 ± 0.004	0.029
intermolecular (172)	0.032 ± 0.007	0.035	0.030 ± 0.006	0.034
intra- and/or intermolecular (82)	0.034 ± 0.007	0.004	0.034 ± 0.010	0.033
calcium ligand (20)	0.003 ± 0.004	0.001	0.003 ± 0.004	0.002
zinc ligand (8/0)[c]	0.048 ± 0.022	0.021	NA	NA
hydrogen bonds (180)	0.027 ± 0.003	0.028	0.025 ± 0.002	0.023
rmsd from experimental dipolar constraints (Hz)				
$^1D_{NH}$ (98)	0.43 ± 0.03	0.41	0.41 ± 0.02	0.43
rmsd from experimental dihedral constraints (deg)[b]				
ϕ and ψ (298)	0.657 ± 0.103	0.554	0.642 ± 0.082	0.697
rmsd from experimental ^{13}C chemical shifts				
$^{13}C\alpha$ (ppm)	1.216 ± 0.031	1.198	1.224 ± 0.037	1.193
$^{13}C\beta$ (ppm)	0.999 ± 0.018	0.985	1.005 ± 0.022	0.998
rmsd from idealized covalent geometry				
bonds (Å)	0.004 ± 0.000	0.004	0.004 ± 0.001	0.004
angles (deg)	0.508 ± 0.012	0.491	0.499 ± 0.016	0.515
impropers (deg)	0.414 ± 0.019	0.400	1.224 ± 0.027	0.413
Lennard−Jones potential energy (kcal/mol)[d]	−849 ± 24	−857	−851 ± 24	−885
percent of residues in the most favorable region of the Ramachandran plot[e]	86.0 ± 1.7	83.7	85.5 ± 2.0	84.9
rmsd to the mean structure (Å)[f]				
ordered backbone atoms (1−88)	0.45 ± 0.08	0.35	0.46 ± 0.10	0.34
ordered heavy atoms (1−88)	1.02 ± 0.08	0.88	1.05 ± 0.09	0.95

[a] The 20 ensemble structures, ⟨20⟩, are the results of simulated annealing calculations. The best structure is closest to the average structure. The values shown for the ⟨20⟩ are the mean ± standard deviation. The force constants used in the refinement are as follows: 1000 kcal mol^{-1} $Å^{-2}$ for the bond length, 500 kcal mol^{-1} rad^{-2} for angles and improper torsions, 4 kcal mol^{-1} $Å^{-4}$ for the quartic van der Waals (vdw) repulsion term (hard-sphere effective vdw set to 0.8 times their values in CHARMm parameters), 50 kcal mol^{-1} $Å^{-2}$ for experimental distance restraints, 150 kcal mol^{-1} rad^{-2} for dihedral constraints, 100 kcal mol^{-1} $Å^{-2}$ for noncrystallographic symmetry, 1 kcal mol^{-1} $Å^{-2}$ for distance symmetry constraints, 0.5 kcal mol^{-1} ppm^{-2} for the ^{13}C chemical-shift constraints, and 1.0 for the conformational database potential. [b] None of the 20 structures has a distance violation >0.4 Å or a dihedral angle violation of >5°. [c] There are 2626 distance restraints when the 8 Zn^{2+} constraints are used but only 2618 distance restraints when Zn^{2+} constraints are not used. [d] Lennard−Jones van der Waals energy was calculated using CHARMm parameters and was not used in any stage of the structure determination. [e] PROCHECK was employed to get the Ramachandran plot. [f] Ordered backbone calculations included C^a, N, and C′ atoms. Only residues 1−88 were included because no long-range NOEs were observed for residues 89−91.

to the BioMagResBank (BMRB) database entry for Zn^{2+}-Ca^{2+}-S100B was made to include all of the new resonance assignments (BMRB accession number 5895).

The tautomerization of the His residues were determined as previously described from the LR-HSQC data (*6*, *58*). The tautomerization state of the histidine residues is important to know for several reasons. First, if a histidine residue shows chemical-shift values for both tautomer states, then it is not "locked" into a single conformation and therefore cannot be a Zn^{2+} ligand. For histidine residues that are ligands to Zn^{2+}, only one tautomerization state should be observed; clearly, these data are important for determining which nitrogen of histidine side chain is not protonated and is therefore free to ligand Zn^{2+}. As seen for Ca^{2+}-S100B, His-25 was found to be the only His residue in the $N_{\epsilon 2}$-H tautomerization state, but its correlations were broadened compared to the Ca^{2+}-S100B LR-HSQC, perhaps as a result of its interaction with Zn^{2+} (*6*). While, only a single correlation was observed for His-85 in the LR-HSQC, $N^{\epsilon 2}$-$N^{\delta 2}$, this correlation has a chemical-shift value similar to the deprotonated imidazole ^{15}N of His-15 and His-25, suggesting that His-85 is also in the $N^{\delta 1}$-H tautomerization state. His-42 and His-90 have significant populations of both the $N^{\epsilon 2}$-H and $N^{\delta 1}$-H tautomerization states because all four of the possible two-bond ^1H-^{15}N His side-chain correlations are observed in the LR-HSQC spectrum. While the two spin systems observed for His-42 slightly favors $N^{\epsilon 2}$-H tautomerization, the H42A mutation does not affect the ability of S100B to bind Zn^{2+} (<2-fold effects) (*6*); therefore, His-42 may favor this tautomerization state by a small amount because of some other interaction. Likewise, the imidazole ring of His-90 in Zn^{2+}-Ca^{2+}-S100B does not lock into one tautomerization state, and like the H42A mutation, the H90A mutation has little or no affect on binding Zn^{2+} (<2-fold).

These results for the His residues in Zn^{2+}-Ca^{2+}-S100B agree well with that predicted previously from mutagenesis, NMR, and modeling studies done with Ca^{2+}-S100B (*6*). Specifically, the chemical-shift perturbations and line-broadening observed for the side-chain His correlations during the Zn^{2+} titration are consistent with three His residues of S100B (H15, H25, and H85) interacting with Zn^{2+} via slow exchange on the chemical-shift time scale, while that His-42 and His-90 are not likely to be Zn^{2+} ligands. The data from the LR-HSQC of Zn^{2+}-Ca^{2+}-S100B also indicate that His-15 and His-85 are in the $N^{\delta 1}$-H tautomerization state and that His-25 is in the $N^{\epsilon 2}$-H tautomerization state. Therefore, the $N^{\epsilon 2}$ of His-15 and His-85 together with the $N^{\delta 1}$ of His-25 are available to directly coordinate Zn^{2+}.

Three-Dimensional NMR Structure of Zn^{2+}-Ca^{2+}-S100B. The solution NMR structure of Zn^{2+}-Ca^{2+}-S100B was determined using 3014 constraints (16.6 per residue; Table

1). This included 478 intraresidue, 576 sequential, 692 medium range, 418 long range, 172 intermolecular, 82 intra- and/or intermolecular NOE correlations, 180 hydrogen bonds, 298 dihedral restraints (ϕ and ψ angles), 20 Ca^{2+} constraints, and 98 $^1D_{NH}$ dipolar constraints; however, no constraints to Zn^{2+} were included in the initial structure calculations. The 20 best structures selected had no NOE violations (>0.4 Å), no dihedral violations (>5°), and had the lowest energy with the majority of residues in the most favorable regions of the Ramachandran diagram (85.5%) with none in the disallowed region (Table 1). The ensemble of these 20 structures have low deviations from the experimental constraints and have an overall rmsd = 1.05 ± 0.09 Å for all heavy atoms and 0.46 ± 0.10 Å for the ordered backbone atoms (i.e., for residues 1−88; Table 1). In addition, the rmsd from the experimental dipolar constraints is 0.41 ± 0.02 Hz and 0.64 ± 0.08° from the dihedral constraints. The ϕ and ψ angle constraints for residues in the typical and pseudo-EF-hand domains were in the expected range as found in other EF-hands, including Ca^{2+}-bound D9K, troponin C, calmodulin, and parvalbumin (*54*).

Zinc-Binding Site in Zn^{2+}-Ca^{2+}-S100B. Support for including eight structural constraints from Zn^{2+} to His-15 and His-25 of one subunit and His-85′ and Glu-89′ of the other S100B is provided by NMR data, ITC data, mutagenesis data, and X-ray structures of other S100 proteins determined previously.

On the basis of mutational analysis of putative Zn^{2+} ligands and homology with the Zn^{2+} site in S100A7, it was originally postulated that His-15 $N^{\epsilon 2}$, His-25 $N^{\delta 1}$, Cys-84′ S^{γ}, and His-85′ $N^{\epsilon 2}$ of S100B coordinate Zn^{2+} in a tetrahedral geometry (*6*). Specifically, the H15A, H25A, C84A, and H85A mutations were found to reduce Zn^{2+} binding by 28-fold, 6-fold, >28-fold, and 12-fold, respectively (*6*). However, upon the completion of the NMR solution structure of Zn^{2+}-Ca^{2+}-S100B without Zn^{2+} constraints, it was clear that Cys-84 is not positioned to be a Zn^{2+} ligand (Figure 2). Specifically, the extension of helix IV and a kink of this helix upon Zn^{2+} binding positions Cys-84 away from the rest of the putative Zn^{2+} ligands (His-15, His-25, and His-85), located in the target-protein-binding cleft. Thus, Cys-84 is not anywhere nearby any of the other putative Zn^{2+}-binding residues, which all lie in a region analogous to the Zn^{2+} and Cu^{2+} site in S100A7 and S100A12, respectively (*6*, *18*). In fact, the Cys-84 side chain may even interact with the target peptides such as TRTK and/or NDR peptide when they bound to S100B (*24*). As further evidence that Cys-84 is not a ligand, it was not possible to generate a reasonable structure using His-15 $N^{\epsilon 2}$, His-25 $N^{\delta 1}$, Cys-84 S^{γ}, and His-85 $N^{\epsilon 2}$ as ligands. In structure calculations that included Cys-84 as a ligand, there were always serious violations in numerous distance and geometry constraints and the final structures resulted in highly distorted geometries for Zn^{2+} coordination. On the other hand, the use of constraints from His-15 $N^{\epsilon 2}$, His-25 $N^{\delta 1}$, and His-85 $N^{\epsilon 2}$ to Zn^{2+}, without constraints to Cys-84, generated low-energy structures that were comparable to structures calculated without Zn^{2+} constraints (Table 1). Therefore, the use of Zn^{2+}-liganding constraints to His-15 $N^{\epsilon 2}$, His-25 $N^{\delta 1}$, and His-85 $N^{\epsilon 2}$ without constraints to Cys-84 S^{γ} is reasonable.

The loss of Zn^{2+} affinity previously observed with the C84A mutation (*6*, *28*) is likely due to conformational changes in the S100B protein from the mutation that affect Zn^{2+} binding indirectly. The HSQC spectrum of the C84A mutant was compared to wild-type S100B to determine if the C84A mutation causes disruption of the overall structure of S100B. Unlike the other mutants of S100B used in these studies (H15A, D23A, H25A, H85A, E89A, and the Δ89−91), which only had localized chemical-shift perturbations spatially nearby the mutation, the C84A mutation residues caused widespread changes throughout the backbone of S100B indicative of a structural perturbation caused by the mutation itself (see Figure 1S in the Supporting Information). The C84A mutation also caused a 4.5-fold decrease in affinity for a peptide derived from the C-terminal of p53 ($p53^{F385W}$) in the absence of Zn^{2+}, suggesting that the mutation affects peptide and/or Ca^{2+} binding in addition to affecting the binding of Zn^{2+} (*6*). While it seems clear that Cys-84 is important to the overall structure of S100B, it is unlikely to be a Zn^{2+} ligand based on the data presented here.

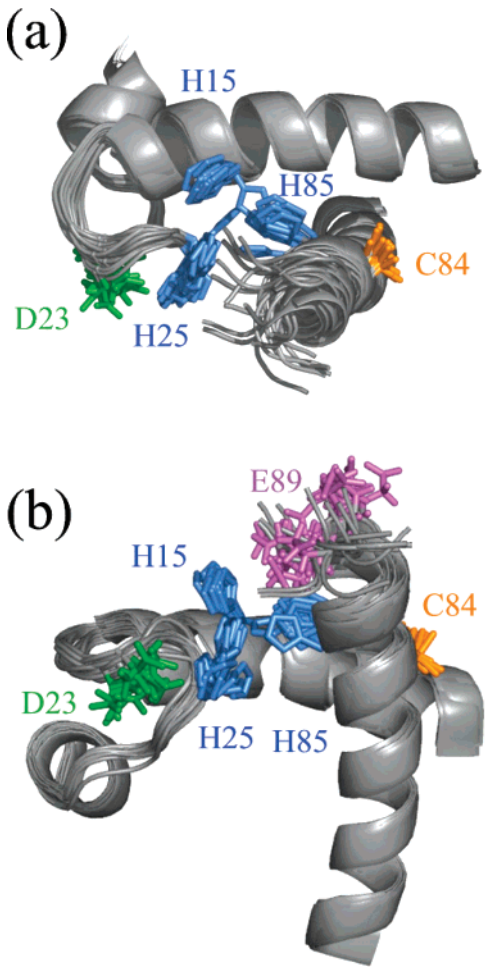

FIGURE 2: Two views of Zn^{2+}-Ca^{2+}-S100B that illustrate putative Zn^{2+} ligands from residues in helix 1, loop 1, and helix 4 of S100B. The 20 structures of Zn^{2+}-Ca^{2+}-S100B used in this figure were calculated without distance constraints to Zn^{2+}. (a) View of the Zn^{2+}-binding site showing the side chains of His-15, His-25, and His-85 (in blue), which are oriented to coordinate Zn^{2+}. On the other hand, Cys-84 (orange) and Asp-23 (green) are both oriented away from the other putative ligands and are not likely to coordinate Zn^{2+}. (b) In another view (90° shifted), in which helix IV is now parallel to the page, the position of Glu-89 (magenta) can be seen. Glu-89 is in a good position to supply the fourth ligand to Zn^{2+} in conjunction with His-15, His-25, and His-85.

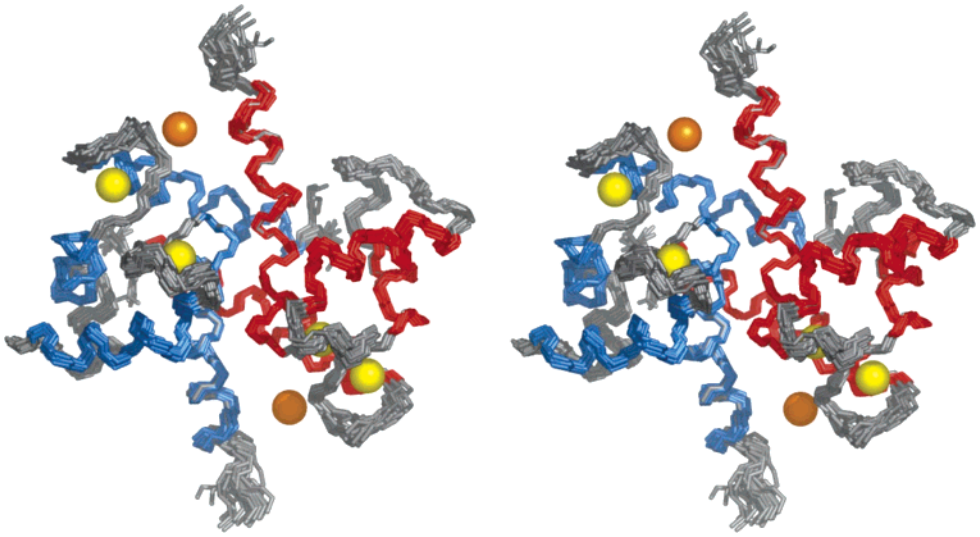

FIGURE 3: Overlay of the 20 best structures for Zn^{2+}-Ca^{2+}-S100B shown in stereoview. The helices of S100B subunits are in blue (helix I−IV) and red (helix I′−IV′), with the Ca^{2+} ions shown in yellow and Zn^{2+} ions shown in orange.

On the basis of Ca^{2+}-Zn^{2+}-S100B structures calculated without constraints to Zn^{2+} and crystal structures for Zn^{2+}-Ca^{2+}-S100A7 and Cu^{2+}-Ca^{2+}-S100A12, several other amino acid residues could potentially be involved in coordinating Zn^{2+} in S100B including Asp-23, Glu-86, Glu-89, and Glu-91 (Figure 2). While Cys and His make up the majority of structural Zn^{2+} sites, the carboxylate oxygen atoms of Asp and Glu are also found to coordinate Zn^{2+} in cocatalytic and catalytic sites (*59*). In S100 proteins, S100A7 has Asp-24 as a bidentate ligand coordinating Zn^{2+} in a trigonal bipyrimidal geometry and S100A12 has Asp-25 as a monodentate ligand to coordinate Cu^{2+} in a tetrahedral geometry (*17*, *18*). In S100B, there is an Asp residue at position 23, which was mutated to determine whether it had an effect on Zn^{2+}-binding affinity. As done previously for all His and Cys residues in S100B (*6*), ITC analysis was used to determine the Zn^{2+} dissociation constant for the D23A mutant, which showed a 10.7-fold decreased affinity for Zn^{2+} ($K_d = 1.00 \pm 0.02$ μM) when compared to wild-type S100B ($K_d = 0.094 \pm 0.016$ μM). Looking at the 20 lowest energy structures determined without constraints to Zn^{2+} shows that Asp-23 is close to the metal site; however, it is not favoring any particular position that would suggest that it is a candidate ligand (Figure 2). While the most conservative interpretation of the mutational data is that Asp-23 is involved directly in binding Zn^{2+}, it is also possible that Asp-23 forms a hydrogen bond to His-25 and properly orients it as a ligand. The most convincing evidence that the latter interpretation is correct is that Asp-23 is not located nearby the Zn^{2+} site in structure calculations done in the absence of Zn^{2+} constraints (Figure 2). Furthermore, it was impossible to generate reasonable structures when distance constraints from Asp-23 were included, as either a monodentate (†) or a bidentate (‡) ligand to Zn^{2+}, in any combination with His-15 $N^{\epsilon 2}$, His-25 $N^{\delta 1}$, and His-85 $N^{\epsilon 2}$. Furthermore, chemical-shift perturbations observed for the D23A mutation affected only a very few residues in S100B, with the largest affect found for His-25. This residue was completely lost because of exchange-broadening effects. For these reasons, it is thought that Asp-23 maybe important in orienting His-25 as a Zn^{2+} ligand and that Asp-23 itself is not directly bound to Zn^{2+}.

There are several C-terminal residues that are capable of coordinating Zn^{2+} including Glu-89, His-90, and Glu-91. However, single-mutational analysis of these residues is complicated because the C terminus is flexible and it is possible that a mutated ligand could be replaced by one of the remaining amino acid residues including even the C-terminal carboxylate and/or carbonyl oxygen atoms. Therefore, a deletion mutant, which removed the final 3 residues of S100B (Δ89−91), was prepared and analyzed by ITC to determine if one or more of these amino acid residues contributes to Zn^{2+} binding. Results from the ITC binding studies indicate that the S100B (Δ89−91) mutant has a 52.2-fold decrease in affinity for Zn^{2+} ($K_d = 5.05 \pm 1.02$ μM) compared to wild-type S100B ($K_d = 0.094 \pm 0.016$ μM). This is a larger effect than that observed for any of the other point mutations studied thus far (H15A decreased 28.2-fold, $K_d = 2.65 \pm 0.88$ μM; H85A decreased 12.4-fold, $K_d = 1.17 \pm 0.79$ μM; and H25A decreased 5.9-fold, $K_d = 0.56 \pm 0.087$ μM) and could be affecting more than one ligand (i.e., perhaps also H85) (*6*). The H90A mutation decreases Zn^{2+} binding to S100B by only 1.9-fold ($K_d = 1.82 \pm 0.01$ μM) (*6*) and is not locked into any one tautomerization state, as mentioned earlier; therefore, it can be ruled out as a possible ligand. Of the remaining 2 amino acids removed in the Δ89−91 mutation, NMR chemical-shift data is consistent with Glu-89 but not Glu-91, forming a ligand to Zn^{2+}. Typically, chemical-shift values for atoms coordinating Zn^{2+} are downfield-shifted, and all of the chemical-shift values and intensity of resonances for Glu-91 are virtually unchanged, which is evidence that oxygen atoms of Glu-91 do not ligand Zn^{2+}. However, when the chemical shifts for Ca^{2+}-S100B and Zn^{2+}-Ca^{2+}-S100B are compared for Glu-89, the values for E89 C^{γ} and H^{γ} are shifted upon Zn^{2+} binding from 36.1 to 36.7 ppm and from 2.08 to 2.43 ppm, respectively. Furthermore, the backbone ^1H and ^{15}N for Glu-89 undergoes exchange broadening upon Zn^{2+} addition, indicating that its local environment has changed. Importantly, mutation of this site (E89A) results in more than a 4-fold loss in binding activity ($K_d = 385 \pm 40$ nM) when compared to that of the wild-type protein, which is a further indication that this residue is a ligand to Zn^{2+}. Therefore, constraints from Zn^{2+} to the side-chain

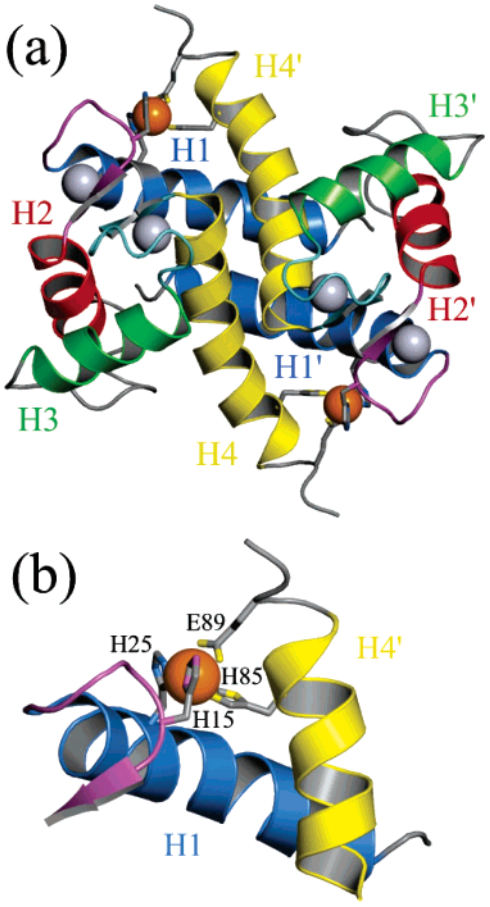

FIGURE 4: Ribbon diagrams of Zn^{2+}-Ca^{2+}-S100B. (a) Ribbon diagram of the best Zn^{2+}-Ca^{2+}-S100B structure illustrating the X-type four-helix bundle comprising the antiparallel helices H1 and H1′ (blue) and H4 and H4′ (yellow). The short antiparallel β sheet between the pseudo- (magenta) and typical (cyan) EF-hand domains is shown as arrows. The pseudo-EF-hand is formed by the loop (magenta) between H1 and H2, and the typical EF-hand is formed by a loop (cyan) between H3 (green) and H4 (yellow). Both are occupied by Ca^{2+} (silver). The target peptides and proteins bind in the hydrophobic cleft formed between H3 and H4 (and H3′/H4′) with many contacts with the flexible "hinge" loop (gray) found between H3 and H2. (b) Close-up showing the Zn^{2+}-binding site in Zn^{2+}-Ca^{2+}-S100B. The Zn^{2+} ions (orange) are coordinated by His15 $N^{\epsilon 2}$ in H1 and His-25 $N^{\delta 1}$ in the pseudo-EF-hand loop of one subunit and with His-85 $N^{\epsilon 2}$ and of †Glu-89 O^{ϵ} from H4′ of the other subunit.

carbonyl of Glu-89 as either a monodentate (†Glu-89 O^{ϵ}) or bidentate (‡Glu-89 O^{ϵ}) ligand were tested in structure calculations together with Zn^{2+} constraints to His-15 $N^{\epsilon 2}$, His-25 $N^{\delta 1}$, and His-85 $N^{\epsilon 2}$. Both combinations of structures using Glu-89 as a ligand yielded similar low-energy structures with reasonable Zn^{2+} coordination geometry, with the monodentate †Glu-89 O^{ϵ} ligand having slightly lower energies than the bidentate ‡Glu-89 O^{ϵ} ligands. Therefore, the final structure calculation included Zn^{2+} constraints, which was necessary to coordinate †Glu-89 O^{ϵ} and His-85 $N^{\epsilon 2}$ from one subunit and His-15 $N^{\epsilon 2}$ and His-25 $N^{\delta 1}$ from the other subunit of Zn^{2+}-Ca^{2+}-S100B. Overall, the inclusion of these eight additional Zn^{2+} constraints (four per Zn^{2+} site) produced high-quality Zn^{2+}-Ca^{2+}-S100B structures that had slightly better statistics than those generated without such Zn^{2+} constraints (Table 1 and Figures 3 and 4). The coordinates for these 20 lowest energy structures are deposited in the Protein Data Bank (PDB code 1XYD).

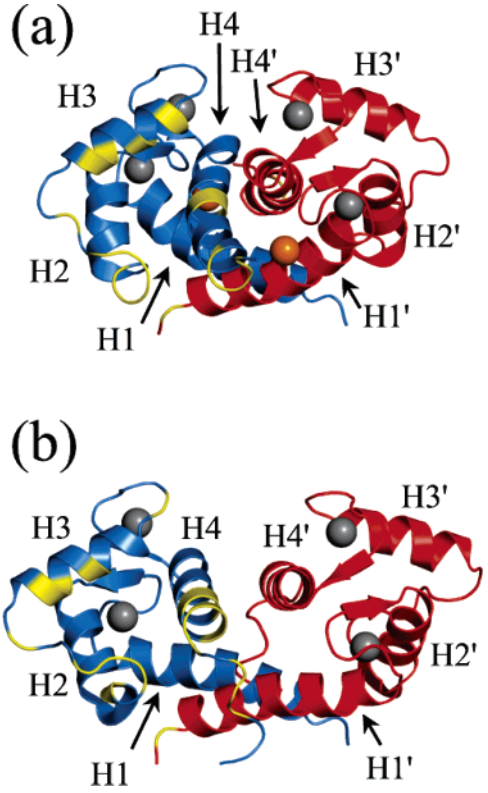

FIGURE 5: Comparison of the target-protein-binding site of S100B in the Zn^{2+}-Ca^{2+}-bound and Ca^{2+}-bound states. (a) Ribbon diagram of Zn^{2+}-Ca^{2+}-S100B highlighting amino acid residues whose backbone ^1H and ^{15}N chemical-shift values are shifted upon binding the $p53^{367-388}$ peptide (yellow) (*6*). (b) Ribbon diagram of Ca^{2+}-S100B highlighting amino acid residues whose backbone ^1H and ^{15}N chemical-shift values are shifted upon binding the $p53^{367-388}$ peptide (yellow) (*5*). In both figures, only one of two peptide-binding sites is shown for simplicity. Subunits of S100B are shown in blue (helix I−IV) and red (helix I′−IV′) with spheres representing the Ca^{2+} (gray) and Zn^{2+} (orange) ions, respectively.

Description of the Overall Structure. With some slight but important structural variations, the overall secondary, tertiary, and quaternary structure of dimeric Zn^{2+}-Ca^{2+}-S100B (Figures 3 and 4) is similar to other S100B structures including apo-S100B, Ca^{2+}-S100B, TRTK-S100B, NDR-S100B, and $p53^{367-388}$-S100B. In all S100B structures, including Zn^{2+}-Ca^{2+}-S100B, the dimer interface comprises an X-type four-helix bundle, with helices I and I′ aligning antiparallel to each other and perpendicular to the antiparallel alignment of the helix IV and IV′ pair (*20*−*25*, *60*). However, there are some noticeable differences between the Zn^{2+}-Ca^{2+}-S100B dimer structure when compared to the other S100B structures. The coordination of Zn^{2+}, which involves two residues from each subunit of S100B (Figure 4), brings the subunits closer together to give a somewhat more compact dimer interface in Zn^{2+}-Ca^{2+}-S100B (Figures 5 and 6). Specifically, helices IV and IV′ in Zn^{2+}-Ca^{2+}-S100B are closer together (8.4 ± 0.1 Å) than in Ca^{2+}-S100B (10.6 ± 0.5 Å) as calculated using Iha version 1.4 (Table 2). In fact, the antiparallel helices (I and I′ and IV and IV′) are closer together in Zn^{2+}-Ca^{2+}-S100B than for all other S100B structures solved to date (apo-, Ca^{2+}-, NDR-, TRTK-, and $p53^{367-388}$-S100B) (Table 2), with the one exception being the interhelical distance between helices I and I′ of the TRTK-S100B complex, which is slightly less (12.8 ± 0.3 Å) than that found for Zn^{2+}-Ca^{2+}-S100B (13.1 ± 0.4 Å;

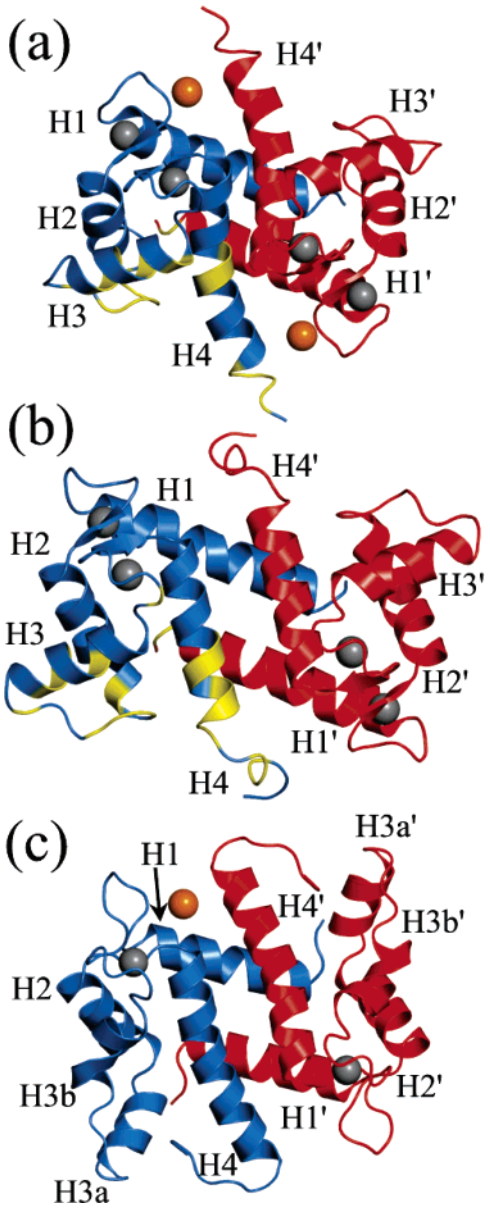

FIGURE 6: Comparison of (a) Zn^{2+}-Ca^{2+}-S100B and (b) Ca^{2+}-S100B with (c) Zn^{2+}-Ca^{2+}-S100A7 (PDB code 3PSR; *17*) with one subunit shown in red and the other in blue, Ca^{2+} in gray, and Zn^{2+} in orange. The amino acid residues whose backbone ^{1}H and ^{15}N chemical-shift values are shifted upon binding the $p53^{367-388}$ peptide (yellow) (*5*, *6*) are shown in yellow as in Figure 5 for (a) Zn^{2+}-Ca^{2+}-S100B and (b) Ca^{2+}-S100B. S100A7 only binds Ca^{2+} in its typical EF-hands, and the crystal structure determined only shows one of the two Zn^{2+}-binding sites occupied. Both the Zn^{2+}-bound S100B and S100A7 structures have a bend in helix 4.

Table 2). For the most part, the dimer interface of S100B is more compact in Zn^{2+}-Ca^{2+}-S100B than in other S100B structures, a characteristic that will likely affect subunit exchange kinetics of heterodimer formation in cells containing multiple S100 proteins.

One interesting feature in the Zn^{2+},Ca^{2+}-bound S100B structure that is absent on all other forms of S100B is a kink (~26°) in the C-terminal α helix (helix IV) starting at Ser-78 (Figure 6). In addition to NOE data, the presence of this kink is supported by $^{1}D_{NH}$ dipolar coupling data, $^{3}J_{HNH\alpha}$ data, and NH exchange data (*6*). Furthermore, this kink is intact whether the Zn^{2+} constraints are included or not. NH exchange data show that two main-chain hydrogen bonds are broken at the kink (S78 and M79), consistent with kinks observed in other proteins (*61*). For S100B, the kink is positioned just where helix IV exits the hydrophobic core and becomes exposed to the solvent as observed for other kinked helices (*61*). Interestingly, it is this solvent-exposed region of helix 4 that interacts directly with target peptides (F76, M79, V80, T82, A83, E86, and F87) (*22*−*24*, *60*).

The EF-Hand Calcium-Binding Sites in Zn^{2+}-Ca^{2+}-S100B. It was found that the conformation of the Ca^{2+}-binding sites shift in position upon the addition of Zn^{2+} to Ca^{2+}-S100B. Specifically, within a subunit, the Ca^{2+} ion in the pseudo- and typical EF-hand move closer together from 14.1 ± 0.6 Å (*21*) in Ca^{2+}-S100B to 12.9 ± 0.4 Å in Zn^{2+}-Ca^{2+}-S100B (Table 2 and Figures 5 and 6); this result is in close agreement with a previous observation using lanthanide luminescence spectroscopy, which showed a change from 15.0 ± 0.4 to 13.0 ± 0.3 Å with the addition of Zn^{2+} (*19*). The two Ca^{2+} ions bound to the typical EF-hands of each subunit also move closer together (~10 Å) from 26.2 ± 1.0 Å apart in Ca^{2+}-S100B to 16.0 ± 0.7 Å upon Zn^{2+} binding. Likewise, the two Ca^{2+} ions bound to the pseudo-EF-hands of each subunit are closer together (~4 Å), going from 38.2 ± 1.2 Å in Ca^{2+}-S100B to 33.7 ± 0.9 Å in Zn^{2+}-Ca^{2+}-S100B. These conformational changes in the EF-hand calcium-binding domains are not unexpected because Zn^{2+} coordination involves a residues in helix 1 (His-15) and the calcium-binding loop (His-25) of the pseudo-EF together with two residues in helix 4 of the typical EF-hand (His-85 and Glu-89). Furthermore, the two EF-hand calcium-binding domains of S100B are themselves connected by a small antiparallel β sheet, so that structural effects that occur in one EF-hand not too surprisingly will affect the structure of the other EF-hand.

In S100B, the interhelical angles (IHAs) between helices I and II and the IHAs between III and IV are important because they contribute to the structure of the pseudo- (I/II) and typical (III/IV) Ca^{2+}-binding EF-hands, and the relative orientations of these pairs of helices likely affect Ca^{2+} ion-binding affinity. For the pseudo-EF-hand, the IHA between helices I and II is not significantly changed by the addition of Zn^{2+} to Ca^{2+}-S100B (Ca^{2+}-S100B, $IHA_{I/II} = 137 \pm 5°$; Zn^{2+}-Ca^{2+}-S100B, $IHA_{I/II} = 131 \pm 2°$; Table 2). For the typical EF-hand, the IHA between helices III and IV changes by ~90° upon binding Ca^{2+}, revealing a hydrophobic binding site need for target protein interaction (*5*, *20*−*23*, *60*, *62*). However, the addition of Zn^{2+} to Ca^{2+}-S100B reverses some of that large conformational change in IHA between III and IV from ~90 to ~79°, closing the binding cleft to some degree. Together, these structural changes in the calcium-binding sites may contribute to the higher affinity that S100B has for Ca^{2+} when Zn^{2+} is bound.

The vector geometry mapping (VGM) method was also used to compare the orientation of the helices forming the EF-hand regions because it is standardized to a reference EF-hand structure allowing for easy comparison among different EF-hand-containing proteins (*63*). Within the different forms of S100B, it was found that the θ values within the pseudo-EF-hand show no clear pattern; however, the φ angles for Zn^{2+}-Ca^{2+}-S100B are most similar to those found for TRTK and $p53^{367-388}$-S100B (Table 3). The trend is identical and more evident in the typical EF-hand with the φ angles becoming nearly the same as values found for the

Table 2: IHAs and Distances of Zn-Ca-S100B Compared to Other S100B, S100A7, and S100A12 Structures[a]

	interhelical angle (deg)								interhelical distance (Å)	
	I−II	I−III	I−IV	II−III	II−IV	III−IV	I−I′	IV−IV′	I−I′	IV−IV′
Zn-Ca-S100B[b]	131.2 ± 1.9	−121.6 ± 1.5	117.2 ± 1.0	105.3 ± 1.5	−34.9 ± 1.2	118.0 ± 1.9	−136.0 ± 2.0	135.0 ± 1.0	12.8 ± 0.4	8.4 ± 0.1
p53-Ca-S100B[c]	120.0 ± 3.0	−123.0 ± 2.0	125.0 ± 1.0	115.0 ± 2.0	−26.0 ± 2.0	110.0 ± 1.0	−152.0 ± 2.0	138.0 ± 2.0	14.1 ± 0.2	10.3 ± 0.2
TRTK-Ca-S100B[d]	132.0 ± 2.0	−118.0 ± 3.0	128.0 ± 1.0	109.0 ± 2.0	−33.0 ± 2.0	108.0 ± 4.0	−148.0 ± 2.0	146.0 ± 3.0	12.4 ± 0.1	9.3 ± 0.3
Ndr-Ca-S100B[e]	141.9 ± 3.3	−118.0 ± 2.9	128.6 ± 1.5	99.8 ± 3.4	−29.8 ± 1.2	108.1 ± 2.9	−154.0 ± 2.0	153.0 ± 0.3	14.2 ± 0.2	9.7 ± 0.3
Ca-S100B[f]	137.0 ± 5.0	−118.0 ± 5.0	128.0 ± 4.0	104.0 ± 3.0	−35.0 ± 4.0	106.0 ± 4.0	−155.0 ± 1.0	159.0 ± 5.0	14.3 ± 0.5	10.6 ± 0.5
apo-S100B[g]	133.0 ± 1.0	−46.0 ± 1.0	120.0 ± 1.0	149.0 ± 1.0	−40.0 ± 1.0	-166.0 ± 1.0	−153.0 ± 1.0	155.0 ± 1.0	13.6 ± 0.3	10.3 ± 0.4
Cu-Ca-S100A12[h]	140.2	−109.9	125.0	115.0	−23.4	121.5	−153.0	146.0	14	9.8
Ca-S100A12[i]	139.6	−106.9	123.6	118.7	−20.4	126.2	−160.0	152.0	14	10.0
Zn-Ca-S100A7[j]	142.6	−93.3	128.2	123.7	−30.2	129.7	−146.0	145.0	13	13.3
Zn-Ca-S100A7[k]	144.5	−91.1	130.4	123.7	−32.9	127.8	NA	NA	NA	NA
Ca-S100A7[l]	145.7	−90.2	131.5	123.4	−30.6	129.7	−146.0	145.0	13	13.1

[a] IHAs were calculated using Interhlx software (K. Yap, University of Toronto) except I to I′ and IV to IV′ IHAs, and interhelical distances were determined using Iha version 1.4 (S. M. Gagne, SMG Software, Inc.) using the helices and structures indicated. [b] Helices for all S100B structures were defined as helix I = 2−18, II = 29−40, III = 50−62, and IV = 70−82. [c] Calculated using PDB entry 1DT7. [d] Calculated using PDB entry 1MWN. [e] Calculated using PDB entry 1PSB. [f] Calculated using PDB entry 1QLK. [g] Calculated using PDB entry 1B4C. [h] Calculated using PDB entry 1ODB, and helices for all S100A12 were defined as helix I = 2−18, II = 29−40, III = 50−60, and IV = 70−82. [i] Calculated using PDB entry 1E8A. [j] Calculated using PDB entry 3PSR, and helices for all S100A7 were defined as helix I = 4−18, II = 28−39, III = 53−61, and IV = 71−90. [k] Calculated using PDB entry 2PSR. [l] Calculated using PDB entry 1PSR.

Table 3: EF-Hand Angles of Zn-Ca-S100B Compared to Other S100B, S100A7, and S100A12 Structures Determined Using the VGM Method[a]

	N-terminal coordinate of second helix			θ (deg)	ϕ (deg)	ω (deg)
			Pseudo-EF-hand			
Zn-Ca-S100B[b]	8.840	2.480	−6.440	46 ± 2	92 ± 3	95 ± 3
p53-Ca-S100B[c]	9.370	−2.265	−6.410	64 ± 4	95 ± 3	113 ± 4
TRTK-Ca-S100B[d]	9.228	−0.837	−7.262	55 ± 2	95 ± 3	97 ± 4
Ndr-Ca-S100B[e]	8.777	−1.171	−6.085	44 ± 4	71 ± 4	129 ± 4
Ca-S100B[f]	10.579	−2.717	−6.722	53 ± 4	80 ± 5	117 ± 7
apo-S100B[g]	11.693	−3.802	−5.592	55 ± 1	89 ± 4	130 ± 5
Cu-Ca-S100A12[h]	8.156	−1.390	−6.537	49	79	118
Ca-S100A12[i]	8.003	−1.652	−6.769	49	76	122
Zn-Ca-S100A7[j]	8.666	0.606	−6.698	45	88	115
Zn-Ca-S100A7[k]	8.543	0.597	−6.517	45	90	111
Ca-S100A7[l]	8.188	1.005	−6.546	43	87	111
			Typical-EF-hand			
Zn-Ca-S100B[b]	10.440	−0.100	−4.690	68 ± 2	110 ± 2	82 ± 3
p53-Ca-S100B[c]	9.823	1.735	−4.808	73 ± 2	112 ± 2	85 ± 3
TRTK-Ca-S100B[d]	9.070	0.973	−5.863	70 ± 4	112 ± 3	66 ± 3
Ndr-Ca-S100B[e]	8.813	−2.117	−4.495	76 ± 3	82 ± 4	109 ± 6
Ca-S100B[f]	10.244	−2.799	−5.997	76 ± 5	95 ± 7	86 ± 10
apo-S100B[g]	8.181	10.267	−4.097	17 ± 1	-122 ± 3	91 ± 3
Cu-Ca-S100A12[h]	8.039	1.321	−6.649	56	97	64
Ca-S100A12[i]	8.298	1.587	−6.437	53	95	69
Zn-Ca-S100A7[j]	9.113	0.478	−6.874	50	98	185
Zn-Ca-S100A7[k]	9.247	0.972	−6.684	51	104	179
Ca-S100A7[l]	9.015	0.630	−6.940	49	99	182

[a] VGM method angles were calculated using VGM software (K. Yap, University of Toronto) using helices and structures indicated. [b] Helices for all S100B structures were defined as helix I = 10−17, II = 29−39, III = 53−60, and IV = 70−80. [c] Calculated using PDB entry 1DT7. [d] Calculated using PDB entry 1MWN. [e] Calculated using PDB entry 1PSB. [f] Calculated using PDB entry 1QLK. [g] Calculated using PDB entry 1B4C. [h] Calculated using PDB entry 1ODB, and helices for all S100A12 were defined as helix I = 10−17, II = 29−39, III = 53−60, and IV = 70−80. [i] Calculated using PDB entry 1E8A. [j] Calculated using PDB entry 3PSR, and helices for all S100A7 were defined as helix I = 12−19, II = 28−38, III = 54−61, and IV = 70−80. [k] Calculated using PDB entry 2PSR. [l] Calculated using PDB entry 1PSR.

p53$^{367-388}$ and TRTK-S100B complexes (Table 3). Overlaying the EF-hands of Zn^{2+}-Ca^{2+}-S100B with the EF-hands of either Ca^{2+}-S100B or the p53$^{367-388}$-S100B complex further reveals the overall similarities of the Ca^{2+}-binding sites in Zn^{2+}-Ca^{2+}-S100B and the peptide-bound structure (Figure 7), and because the p53$^{367-388}$-S100B complex also increases in Ca^{2+} affinity (2.7-fold) (*5*), these similar arrangements of the Ca^{2+}-binding sites may be partially responsible for the increased affinity. This result suggests that Zn^{2+} binding contributes to pre-forming of the S100B protein into a conformation that is better suited to associate with calcium and/or target proteins/peptides.

Target-Protein-Binding Site in Zn^{2+}-Ca^{2+}-S100B. It is well-recognized that the binding of target peptides to holo-S100B involves residues in loop 2 (hinge region), helix 3, helix 4, and the C-terminal loop (*22*−*24*, *60*, *64*). This is also the case for Zn^{2+}-Ca^{2+}-S100B upon the addition on target peptides such as p53$^{367-388}$ or TRTK-12 as determined by monitoring HSQC chemical-shift perturbations (Figure 5). For Ca^{2+}-S100B, the binding of such peptides to holo-S100B also extends the length of helix 4 by four or five residues (*22*, *23*, *62*), which is not the case for Zn^{2+}-Ca^{2+}-S100B because helix 4 is already preformed by the addition of Zn^{2+} alone. Therefore, it is not surprising that chemical-

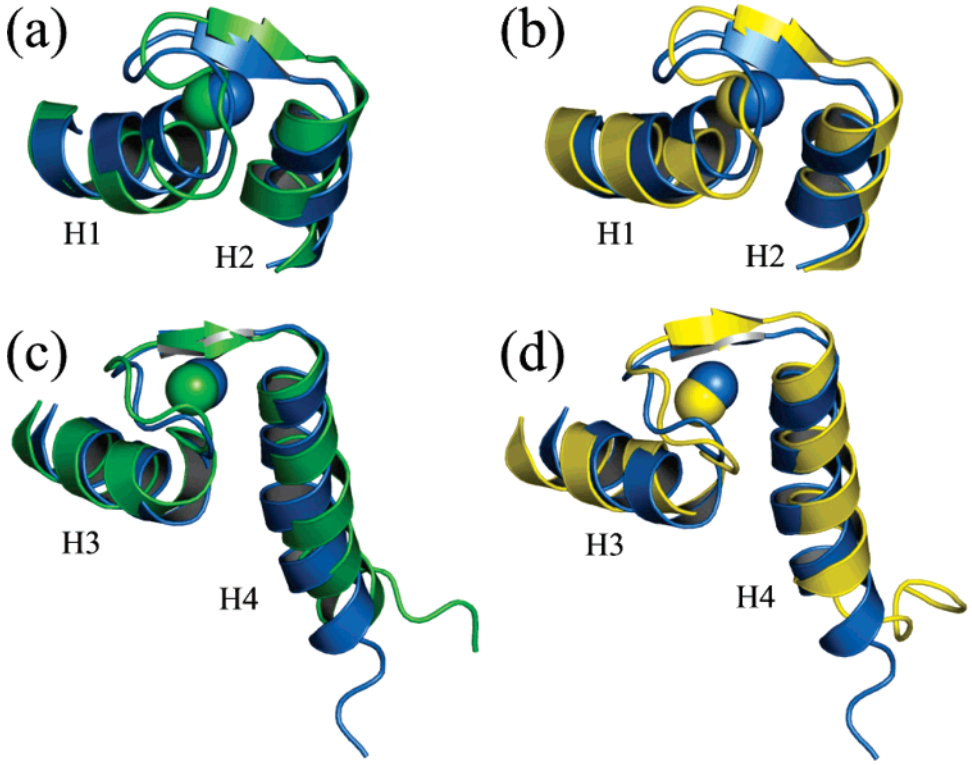

FIGURE 7: Comparison of the pseudo-EF-hand (a and b) and typical EF-hand (c and d) calcium-binding domains of Zn^{2+}-Ca^{2+}-S100B (blue) with those in Ca^{2+}-S100B (yellow) or $p53^{367-388}$-Ca^{2+}-S100B (green). (a) Overlay of the pseudo-EF-hand of Zn^{2+}-Ca^{2+}-S100B (blue) with the pseudo-EF-hand domain of $p53^{367-388}$-Ca^{2+}-S100B (green). (b) Overlay of the pseudo-EF-hand of Zn^{2+}-Ca^{2+}-S100B (blue) with the pseudo-EF-hand domain of Ca^{2+}-S100B (yellow). (c) Overlay of the typical EF-hand of Zn^{2+}-Ca^{2+}-S100B (blue) with the typical EF-hand domain of the Ca^{2+}-S100B-$p53^{367-388}$ peptide complex (green). (d) Overlay of the typical EF-hand of Zn^{2+}-Ca^{2+}-S100B (blue) with the typical EF-hand domain of Ca^{2+}-S100B (yellow). Conformational changes in the pseudo- and typical EF-hands occur upon Zn^{2+} binding to Ca^{2+}-S100B (b and d) causing the EF-hand domains in Zn^{2+}-Ca^{2+}-S100B to become oriented very similar to the respective EF-hand domains in $p53^{367-388}$-Ca^{2+}-S100B (a and c).

shift perturbations for the last few residues of Ca^{2+}-S100B (residues 85−91) are a bit larger than those observed for Ca^{2+}-Zn^{2+}-S100B (*6*). This occurs because these C-terminal residues become helical and directly interact with the target peptide in Ca^{2+}-S100B titrations, whereas the chemical-shift perturbations arise only from the direct interaction with the peptide in the Ca^{2+}-Zn^{2+}-S100B titrations.

For the $p53^{367-388}$ peptide, Phe-385 and Lys-386 of the peptide interacts with Phe-87 and Glu-86 of Ca^{2+}-S100B (*22*) and the NDR-S100B structure shows that Leu-84 and Leu-86 of NDR interacts with Phe-87 and Ala-83 of S100B, respectively (*24*). Similarly, the TRTK-S100B structure shows that Val-80, Ala-83, and Cys-84 of S100B interacts with the peptide (*23*, *60*). Mutational analysis has also shown the C-terminal region to be important for TRTK binding. Specifically, the F88A and the double F87A/F88A mutant of S100B caused a 4- and 7-fold decrease in TRTK affinity, respectively (*64*), and the deletion of the last seven residues of S100B disrupts helix IV and drastically decreases the proteins affinity for TRTK, with the K_d going from 0.27 ± 0.03 to 659.7 ± 119.3 μM (*60*, *64*). Therefore, it is important to note that the addition of Zn^{2+} to Ca^{2+}-S100B causes changes in the structure of the S100B in regions involved in binding protein targets, such as helix III, helix IV, and the C-terminal loop. Particularly noteworthy is the fact that the Zn^{2+}-dependent conformational change extends helix IV and reorients several residues that comprise the peptide-binding site, including Ala-83, Cys-84, Phe-87, and Phe-88, forcing them to become more structured and face the target-peptide-binding cleft. It is these structural changes that are likely the reason that the TRTK-12 peptide binds Zn^{2+}-Ca^{2+}-S100B 5-fold more tightly than Ca^{2+}-S100B (*8*).

Comparison of Zn^{2+}-Ca^{2+}-S100B with Zn^{2+}-Ca^{2+}-S100A7 and Cu^{2+}-Ca^{2+}-S100A12. Upon binding Zn^{2+}, Ca^{2+}-bound S100B undergoes more pronounced changes in structure than either S100A7 or S100A12. Specifically, the IHA (Table 2) and VGM angle values (Table 3) are virtually unchanged when comparing the crystal structures of Ca^{2+}-S100A7 and Ca^{2+}-S100A12 to their Zn^{2+}- and Cu^{2+}-bound structures, respectively. For S100A7, the loop region of the pseudo-EF-hand rearranges to some degree upon binding Zn^{2+}, but it is not clear that this change is important because this EF-hand does not bind Ca^{2+} (*17*). The typical EF-hand domains of Ca^{2+}-S100A7 were found to move closer together, from 27.8 to 28.7 Å upon Zn^{2+} binding (*17*), but this movement is small in comparison with that observed for S100B, in which the typical two EF-hand domains move by ~5 Å. For S100A12, helix IV is extended by several residues upon binding Cu^{2+} as was also seen when Zn^{2+} binds Ca^{2+}-S100B, although there were no other changes observed in Ca^{2+}-S100A12 upon Cu^{2+} binding (*18*). This lack of a conformational change in the Ca^{2+}-binding sites of S100A12 is particularly unexpected because this S100 protein has a 1500-fold increase in Ca^{2+} affinity upon binding Zn^{2+} (*11*). Nonetheless, it is possible that the conformational changes in S100A12 are very subtle and/or that they only occur with Zn^{2+} binding and not interactions with Cu^{2+}.

CONCLUSIONS

Comparisons of the Zn^{2+}-Ca^{2+}-S100A7, Cu^{2+}-Ca^{2+}-S100A12, and Zn^{2+}-Ca^{2+}-S100B structures illustrate that there is a conserved Zn^{2+} (or Cu^{2+}) metal-ion-binding site in several S100 proteins that is distinct from the EF-hand Ca^{2+}-binding sites (Figure 6). In these S100 proteins, Zn^{2+} (or Cu^{2+}) binds to opposite ends of the S100 protein dimer at the subunit interface in a symmetric manner. The overall tertiary/quaternary fold of Zn^{2+}-Ca^{2+}-S100B is similar to that of Ca^{2+}-S100B; however, specific differences with respect to EF-hand IHAs plus an extension and kink in helix IV upon binding Zn^{2+} are observed. Such changes in S100B structure can be explained by Zn^{2+} ligands from residues in helix I (His-15) and the pseudo-EF-hand (His-25) of one subunit and from residues in the C-terminal loop (His-85 and Glu-89) of the other subunit. It is these changes in conformation that likely modulate how Zn^{2+} affects both Ca^{2+} and target-protein-binding affinity in S100B.

SUPPORTING INFORMATION AVAILABLE

Combined backbone ^1H and ^{15}N chemical-shift perturbations plotted for each amino acid residue to monitor changes in wild-type S100B caused by the H15A, D23A, H25, C84A, H85A, E89A, or Δ89−91 mutations, monitored using the HSQC experiment. This material is available free of charge via the Internet at http://pubs.acs.org.

REFERENCES

1. Kligman, D., and Hilt, D. (1988) The S100 protein family, *Trends Biochem. Sci. 13*, 437−443.
2. Amburgey, J. C., Abildgaard, F., Starich, M. R., Shah, S., Hilt, D. C., and Weber, D. J. (1995) ^1H, ^{13}C, and ^{15}N NMR assignments and solution secondary structure of rat apo-S100B, *J. Biomol. NMR 6*, 171−179.
3. Weber, D. J., Rustandi, R. R., Carrier, F., and Zimmer, D. B. (2000) *Interaction of Dimeric S100B(ββ) with the Tumor Suppressor Protein: A Model for Ca^{2+}-Dependent S100-Target Protein Interactions*, Kluwer Academic Publishers, Dordrecht, The Netherlands.
4. Berridge, M. J., Bootman, M. D., and Roderick, H. L. (2003) Calcium signaling: Dynamics, homeostasis, and remodeling, *Nat. Rev. Mol. Cell. Biol. 4*, 517−529.
5. Rustandi, R. R., Drohat, A. C., Baldisseri, D. M., Wilder, P. T., and Weber, D. J. (1998) The Ca^{2+}-dependent interaction of S100B with a peptide derived from p53, *Biochemistry 37*, 1951−1960.
6. Wilder, P. T., Baldisseri, D. M., Udan, R., Vallely, K. M., and Weber, D. J. (2003) Location of the Zn^{2+}-binding site on S100B as determined by NMR spectroscopy and site-directed mutagenesis, *Biochemistry 42*, 13410−13421.
7. Baudier, J., and Gerard, D. (1986) Ions binding to S100 proteins. II. Conformational studies and calcium-induced conformational changes in S100A1 protein: The effect of acidic pH and calcium incubation on subunit exchange in S100A1 protein, *J. Biol. Chem. 261*, 8204−8212.
8. Barber, K. R., McClintock, K. A., Jamieson, G. A., Jr., Dimlich, R. V., and Shaw, G. S. (1999) Specificity and Zn^{2+} enhancement of the S100B binding epitope TRTK-12, *J. Biol. Chem. 274*, 1502−1508.
9. Gentil, B. J., Delphin, C., Mbele, G. O., Deloulme, J. C., Ferro, M., Garin, J., and Baudier, J. (2001) The giant protein AHNAK is a specific target for the calcium- and zinc-binding S100B protein: Potential implications for Ca^{2+} homeostasis regulation by S100B, *J. Biol. Chem. 276*, 23253−23261.
10. Franz, C., Durussel, I., Cox, J. A., Schafer, B. W., and Heizmann, C. W. (1998) Binding of Ca^{2+} and Zn^{2+} to human nuclear S100A2 and mutant proteins, *J. Biol. Chem. 273*, 18826−18834.
11. Dell'Angelica, E. C., Schleicher, C. H., and Santome, J. A. (1994) Primary structure and binding properties of calgranulin C, a novel S100-like calcium-binding protein from pig granulocytes, *J. Biol. Chem. 269*, 28929−28936.
12. Baudier, J., Glasser, N., and Gerard, D. (1986) Ions binding to S100 proteins. I. Calcium- and zinc-binding properties of bovine brain S100A1, S100 (α β), and S100B protein: Zn^{2+} regulates Ca^{2+} binding on S100B protein, *J. Biol. Chem. 261*, 8192−8203.
13. Heierhorst, J., Mitchelhill, K. I., Mann, R. J., Tiganis, T., Czernik, A. J., Greengard, P., and Kemp, B. E. (1999) Synapsins as major neuronal Ca^{2+}/S100A1-interacting proteins, *Biochem. J. 344* (part 2), 577−583.
14. Raftery, M. J., Harrison, C. A., Alewood, P., Jones, A., and Geczy, C. L. (1996) Isolation of the murine S100 protein MRP14 (14 kDa migration-inhibitory-factor-related protein) from activated spleen cells: Characterization of post-translational modifications and zinc binding, *Biochem. J. 316* (part 1), 285−293.
15. Kerkhoff, C., Vogl, T., Nacken, W., Sopalla, C., and Sorg, C. (1999) Zinc binding reverses the calcium-induced arachidonic acid-binding capacity of the S100A8/A9 protein complex, *FEBS Lett. 460*, 134−138.
16. Sohnle, P. G., Hunter, M. J., Hahn, B., and Chazin, W. J. (2000) Zinc-reversible antimicrobial activity of recombinant calprotectin (migration inhibitory factor-related proteins 8 and 14), *J. Infect. Dis. 182*, 1272−1275.
17. Brodersen, D. E., Nyborg, J., and Kjeldgaard, M. (1999) Zinc-binding site of an S100 protein revealed. Two crystal structures of Ca^{2+}-bound human psoriasin (S100A7) in the Zn^{2+}-loaded and Zn^{2+}-free states, *Biochemistry 38*, 1695−1704.
18. Moroz, O. V., Antson, A. A., Grist, S. J., Maitland, N. J., Dodson, G. G., Wilson, K. S., Lukanidin, E., and Bronstein, I. B. (2003) Structure of the human S100A12-copper complex: Implications for host-parasite defense, *Acta. Crystallogr., Sect. D 59*, 859−867.
19. Chaudhuri, D., Horrocks, W. D., Jr., Amburgey, J. C., and Weber, D. J. (1997) Characterization of lanthanide ion binding to the EF-hand protein S100 β by luminescence spectroscopy, *Biochemistry 36*, 9674−9680.
20. Drohat, A. C., Tjandra, N., Baldisseri, D. M., and Weber, D. J. (1999) The use of dipolar couplings for determining the solution structure of rat apo-S100B, *Protein Sci. 8*, 800−809.
21. Drohat, A. C., Baldisseri, D. M., Rustandi, R. R., and Weber, D. J. (1998) Solution structure of calcium-bound rat S100B as determined by nuclear magnetic resonance spectroscopy, *Biochemistry 37*, 2729−2740.
22. Rustandi, R. R., Baldisseri, D. M., and Weber, D. J. (2000) Structure of the negative regulatory domain of p53 bound to S100B, *Nat. Struct. Biol. 7*, 570−574.
23. Inman, K. G., Yang, R., Rustandi, R. R., Miller, K. E., Baldisseri, D. M., and Weber, D. J. (2002) Solution NMR structure of S100B bound to the high-affinity target peptide TRTK-12, *J. Mol. Biol. 324*, 1003−1014.
24. Bhattacharya, S., Large, E., Heizmann, C. W., Hemmings, B., and Chazin, W. J. (2003) Structure of the Ca^{2+}/S100B/NDR kinase peptide complex: Insights into S100 target specificity and activation of the kinase, *Biochemistry 42*, 14416−14426.
25. Drohat, A. C., Amburgey, J. C., Abildgaard, F., Starich, M. R., Baldisseri, D., and Weber, D. J. (1996) Solution structure of rat apo-S100B as determined by NMR spectroscopy, *Biochemistry 35*, 11577−11588.
26. Chou, J. J., Gaemers, S., Howder, B., Louis, J. M., and Bax, A. (2001) A simple apparatus for generating stretched polyacrylamide gels, yielding uniform alignment of proteins and detergent micelles, *J. Biomol. NMR 21*, 377−382.
27. Chou, J. J., Kaufman, J. D., Stahl, S. J., Wingfield, P. T., and Bax, A. (2002) Micelle-induced curvature in a water-insoluble HIV-1 Env peptide revealed by NMR dipolar coupling measurement in stretched polyacrylamide gel, *J. Am. Chem. Soc. 124*, 2450−2451.
28. Wilder, P. T., Baldisseri, D., Udan, R., Vallely, K. M., and Weber, D. J. (2003) Location of the Zn^{2+}-binding site on S100B as determined by NMR spectroscopy and site-directed mutagenesis, *Biochemistry 42*, 13410−13421.
29. Marion, D., Driscoll, P. C., Kay, L. E., Wingfield, P. T., Bax, A., Gronenborn, A. M., and Clore, G. M. (1989) Overcoming the overlap problem in the assignment of ^1H NMR spectra of larger proteins by use of three-dimensional heteronuclear ^1H-^{15}N Hartmann−Hahn−multiple quantum coherence and nuclear Overhauser−multiple quantum coherence spectroscopy: Application to interleukin 1 β, *Biochemistry 28*, 6150−6156.

30. Bax, A., and Ikura, M. (1991) An efficient 3D NMR technique for correlating the proton and ^{15}N backbone amide resonances with the α-carbon of the preceding residue in uniformly $^{15}N/^{13}C$ enriched proteins, *J. Biomol. NMR 1*, 99−104.
31. Delaglio, F., Grzesiek, S., Vuister, G. W., Zhu, G., Pfeifer, J., and Bax, A. (1995) NMRPipe: A multidimensional spectral processing system based on UNIX pipes, *J. Biomol. NMR 6*, 277−293.
32. Zhu, G., and Bax, A. (1992), Two-dimensional linear prediction for signals truncated in both dimensions, *J. Magn. Reson. 98*, 192−199.
33. Zhu, G., and Bax, A. (1990), Improved linear prediction for truncated signals of known phase, *J. Magn. Reson. 90*, 405−410.
34. Edison, A. S., Abildgaard, F., Westler, W. M., Mooberry, E. S., and Markley, J. L. (1994) Practical introduction to theory and implementation of multinuclear, multidimensional nuclear magnetic resonance experiments, *Methods Enzymol. 239*, 3−79.
35. Live, D. H., Davis, D. G., Agosta, W. C., and Cowburn, D. (1984) Longe range hydrogen bond mediated effects in peptides: ^{15}N NMR study of gramicidin S in water and organic solvents, *J. Am. Chem. Soc*, 1939−1941.
36. Spera, S., Ikura, M., and Bax, A. (1991) Measurement of the exchange rates of rapidly exchanging amide protons: Application to the study of calmodulin and its complex with a myosin light chain kinase fragment, *J. Biomol. NMR 1*, 155−165.
37. Mori, S., Abeygunawardana, C., Johnson, M. O., and van Zijl, P. C. (1995) Improved sensitivity of HSQC spectra of exchanging protons at short interscan delays using a new fast HSQC (FHSQC) detection scheme that avoids water saturation, *J. Magn. Reson. B 108*, 94−98.
38. Pelton, J. G., Torchia, D. A., Meadow, N. D., and Roseman, S. (1993) Tautomeric states of the active-site histidines of phosphorylated and unphosphorylated IIIGlc, a signal-transducing protein from *Escherichia coli*, using two-dimensional heteronuclear NMR techniques, *Protein Sci. 2*, 543−558.
39. Ikura, M., Bax, A., Clore, G. M., and Groneborn, A. M. (1990) Detection of nuclear Overhauser effects between degenerate amide proton resonances by heteronuclear three-dimensional nuclear magnetic resonance spectroscopy, *J. Am. Chem. Soc. 112*, 9020−9022.
40. Kuboniwa, H., Grzesiek, S., Delaglio, F., and Bax, A. (1994) Measurement of HN−H α J couplings in calcium-free calmodulin using new 2D and 3D water-flip-back methods, *J. Biomol. NMR 4*, 871−878.
41. Ottiger, M., Delaglio, F., and Bax, A. (1998) Measurement of J and dipolar couplings from simplified two-dimensional NMR spectra, *J. Magn. Reson. 131*, 373−378.
42. Grzesiek, S., and Bax, A. (1992) Correlating backbone amide and side chain resonances in larger proteins by multiple relayed triple resonance NMR, *J. Am. Chem. Soc. 114*, 6291−6293.
43. Wittekind, M., and Mueller, L. (1993) HNCACB, a high-sensitivity 3D NMR experiment to correlate amide-proton and nitrogen resonances with the α- and *β*-carbon resonances in proteins, *J. Magn. Reson. B 101*, 201−205.
44. Kay, L. E., Ikura, M., Tschudin, R., and Bax, A. (1990) Three-dimensional triple-resonance NMR spectroscopy of isotopically enriched proteins, *J. Magn. Reson. 89*, 496−514.
45. Grzesiek, S., Anglister, J., and Bax, A. (1993) Correlation of backbone amide and aliphatic side-chain resonances in $^{13}C/^{15}N$-enriched proteins by isotropic mixing of ^{13}C magnetization, *J. Magn. Reson. B 101*, 114−119.
46. Muhandiram, D. R., Guang, Y. X., and Kay, L. E. (1993) An enhanced-sensitivity pure absorption gradient 4D $^{15}N,^{13}C$-edited NOESY experiment, *J. Biomol. NMR 3*, 463−470.
47. Vuister, G. W., Clore, G. M., Gronenborn, A. M., Powers, R., Garrett, D. S., Tschudin, R., and Bax, A. (1993) Increased resolution and improved spectral quality in four-dimensional $^{13}C/^{13}C$ separated HMQC−NOESY−HMQC spectra using pulsed field gradients, *J. Magn. Reson. B 101*, 210−213.
48. Bax, A., and Pochapsky, S. S. (1992) Optimized recording of heteronuclear multidimensional NMR spectra using pulsed field gradients, *J. Magn. Reson. 99*, 638−643.
49. Clore, G. M., Nilges, M., Sukumaran, D. K., Brunger, A. T., Karplus, M., and Gronenborn, A. M. (1986) The three-dimensional structure of α-purothionin in solution: Combined use of nuclear magnetic resonance, distance geometry, and restrained molecular dynamics, *EMBO J. 5*, 2729−2735.
50. Clore, G. M., Gronenborn, A. M., Nilges, M., and Ryan, C. A. (1987) Three-dimensional structure of potato carboxypeptidase inhibitor in solution. A study using nuclear magnetic resonance, distance geometry, and restrained molecular dynamics, *Biochemistry 26*, 8012−8023.
51. Wuthrich, K. (1986) *NMR of Proteins and Nucleic Acids*, John Wiley, New York.
52. Clore, G. M., Gronenborn, A. M., and Bax, A. (1998) A robust method for determining the magnitude of the fully asymmetric alignment tensor of oriented macromolecules in the absence of structural information, *J. Magn. Reson. 133*, 216−221.
53. Cornilescu, G., Delaglio, F., and Bax, A. (1999) Protein backbone angle restraints from searching a database for chemical shift and sequence homology, *J. Biomol. NMR 13*, 289−302.
54. Strynadka, N. C., and James, M. N. (1989) Crystal structures of the helix-loop-helix calcium-binding proteins, *Annu. Rev. Biochem. 58*, 951−998.
55. Matsumura, H., Shiba, T., Inoue, T., Harada, S., and Kai, Y. (1998) A novel mode of target recognition suggested by the 2.0 Å structure of holo S100B from bovine brain, *Structure 6*, 233−241.
56. Schwieters, C. D., Kuszewski, J. J., Tjandra, N., and Marius Clore, G. (2003) The Xplor-NIH NMR molecular structure determination package, *J. Magn. Reson. 160*, 65−73.
57. Harding, M. M. (2001) Geometry of metal−ligand interactions in proteins, *Acta Crystallogr., Sect. D 57*, 401−411.
58. Drohat, A. C., Jagadeesh, J., Ferguson, E., and Stivers, J. T. (1999) Role of electrophilic and general base catalysis in the mechanism of *Escherichia coli* uracil DNA glycosylase, *Biochemistry 38*, 11866−11875.
59. McCall, K. A., Huang, C., and Fierke, C. A. (2000) Function and mechanism of zinc metalloenzymes, *J. Nutr. 130*, 1437S−1446S.
60. McClintock, K. A., and Shaw, G. S. (2003) A novel S100 target conformation is revealed by the solution structure of the Ca^{2+}-S100B-TRTK-12 complex, *J. Biol. Chem. 278*, 6251−6257.
61. Kumar, S., and Bansal, M. (1998) Geometrical and sequence characteristics of α-helices in globular proteins, *Biophys. J. 75*, 1935−1944.
62. Rustandi, R. R., Baldisseri, D. M., Drohat, A. C., and Weber, D. J. (1999) Structural changes in the C-terminus of Ca^{2+}-bound rat S100B upon binding to a peptide derived from the C-terminal regulatory domain of p53, *Protein Sci. 8*, 1743−1751.
63. Yap, K. L., Ames, J. B., Swindells, M. B., and Ikura, M. (1999) Diversity of conformational states and changes within the EF-hand protein superfamily, *Proteins 37*, 499−507.
64. McClintock, K. A., van Eldik, L. J., and Shaw, G. S. (2002) The C-terminus and linker region of S100B exert dual control on protein−protein interactions with TRTK-12, *Biochemistry 41*, 5421−5428.

BI0475830